Tuning mechanical modes and influence of charge screening in nanowire resonators

Hari S. Solanki,[1] Shamashis Sengupta,[1] Sajal Dhara,[1] Vibhor Singh,[1] Sunil Patil,[1] Rohan Dhall,[1] Jeevak Parpia,[2] Arnab Bhattacharya,[1] and Mandar M. Deshmukh[1,*]

[1]*Department of Condensed Matter Physics and Materials Science, Tata Institute of Fundamental Research, Homi Bhabha Road, Mumbai 400005, India*

[2]*LASSP, Cornell University, Ithaca, New York 14853, USA*

(Received 24 August 2009; revised manuscript received 24 February 2010; published 29 March 2010)

We probe electromechanical properties of InAs nanowire (diameter ~100 nm) resonators where the suspended nanowire is also the active channel of a field-effect transistor. We observe and explain the nonmonotonic dispersion of the resonant frequency with dc gate voltage (V_g^{dc}). The effect of electronic screening on the properties of the resonator can be seen in the amplitude. We observe the mixing of mechanical modes with V_g^{dc}. We also experimentally probe and quantitatively explain the hysteretic nonlinear properties, as a function of V_g^{dc}, of the resonator using the Duffing equation.

DOI: 10.1103/PhysRevB.81.115459 PACS number(s): 85.85.+j, 62.23.Hj, 77.65.Fs

I. INTRODUCTION

Nanoelectromechanical systems (NEMS) (Ref. 1) are being used extensively to study small displacements,[2] mass sensing,[3–6] spin-torque effect,[7] charge sensing,[8] Casimir force,[9] and potential quantum-mechanical devices.[10,11] A variety of NEMS devices, fabricated using carbon nanotubes,[12–16] graphene,[17–19] nanowires (NWs) of silicon[20] and by micromachining bulk silicon,[21] have been used to probe the underlying physics at nanoscale. In this work we study the electromechanical properties of doubly clamped suspended *n*-type InAs NWs. In our suspended NW field-effect transistor (FET), the gate electrode serves three purposes: first, to modify the tension in the NW, second, to actuate the mechanical motion of the resonator, and third, enabling us to systematically study the coupling of mechanical properties to the tunable electron density. As we will show, a tunable electron density leads to a variable screening length on the order of the nanowire's cross-sectional dimensions. Thus the electromechanical properties enter into a mesoscale regime. Such a variable electron density is not accessible in carbon nanotubes; the screening length cannot be tuned continuously—relative to the diameter of the carbon nanotube—as easily. However, the physics of charge screening in nanoscale capacitors[22] and ferroelectric devices[23] is intimately connected to that in our NEMS devices. Taken together, these observations suggest that a geometrical interpretation of capacitance is inadequate at the nanoscale. Additionally, the gate allows us to tune the resonant frequency nonmonotonically due to the competition between the electrostatic force and the mechanical stiffness (~1 N/m) of the nanowire, a feature expected (but heretofore not studied in detail) for all electrostatically actuated NEMS. In this paper, we demonstrate that the InAs semiconducting nanowire system manifests this transition from softening to hardening as the gate voltage is varied. In addition, mixing of the natural mechanical modes as a function of V_g^{dc} can be understood in terms of the structural asymmetries in the resonator. In the nonlinear regime we study in detail hysteretic behavior as a function of V_g^{dc} (unlike the commonly studied response as a function of drive frequency) and we show that this can be understood by using the Duffing equation incorporating the effect of gate voltage. The observed hysteretic response with V_g^{dc} is an alternate knob for tuning the nonlinear response of our NEMS devices and can be used for charge detection.[24] Our work provides further understanding of the unique characteristics of NEMS devices operating at room temperature. The observed behavior can provide information on the nanomechanics of other systems whose electron density, stiffness, or screening length cannot be so readily tuned.

II. FABRICATION OF DEVICES AND EXPERIMENTAL TECHNIQUE

The InAs NWs used for this work were grown using metal organic vapor phase epitaxy.[25,26] The NWs are oriented in the ⟨111⟩ direction and are 80–120 nm in diameter with a length of several micrometers. The substrate used for making the devices is a degenerately doped silicon wafer with 300-nm-thick SiO_2. We have fabricated suspended InAs NW devices by sandwiching the NWs between two layers of electron-beam resist and then using electron-beam lithography to define the electrodes and suspend them by depositing ~150 nm Cr and ~250 nm Au after development followed by *in situ* plasma cleaning.[26] The Ohmic contacts also serve as mechanical supports for the NW suspended ~200 nm above the surface of SiO_2. Figure 1(a) shows the scanning electron microscope (SEM) image of a resonator device and scheme for actuating and detecting the motion of the resonator. All the measurements were done at 300 K and pressure less than 1 mBar.

To actuate and detect the resonance we use the device as a heterodyne mixer.[6,12,18,27–29] We use electrostatic interaction between the wire and gate to actuate the motion in a plane perpendicular to the substrate. We apply a radio frequency (RF) signal $V_g(\omega)$ and a dc voltage V_g^{dc} at the gate terminal using bias-tee. Another RF signal $V_{SD}(\omega+\Delta\omega)$ is applied to the source electrode [Fig. 1(a)]. The RF signal applied at the gate $V_g(\omega)$ modulates the gap between NW and substrate at angular frequency ω, and V_g^{dc} alters the overall tension in the NW. The amplitude of the current through

 ©2010 The American Physical Society

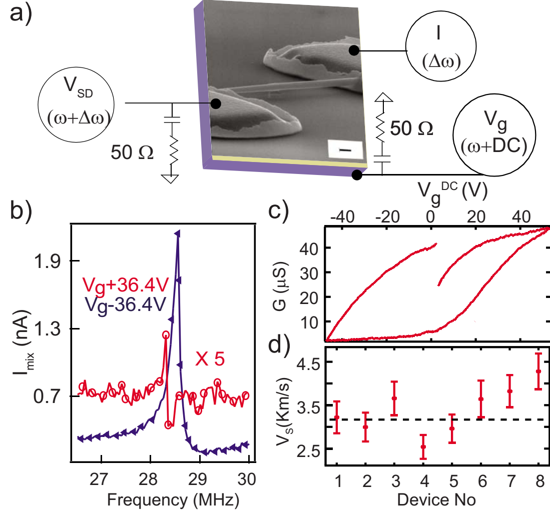

FIG. 1. (Color online) (a) Tilted-angle SEM image with the circuit used for actuation and detection of resonance for an InAs NW resonator. The diameter of the wire is 100 nm and the length of NW is 2.9 μm. The scale bar indicates a length of 200 nm. (b) The mixing current ($\Delta\omega/2\pi$=17 KHz) as a function of frequency for two values of V_g^{dc} (red circles for positive V_g^{dc} and blue triangles for negative V_g^{dc}, mixing current shown for positive V_g^{dc}, is five times of its original value). (c) Variation in the conductance as a function of dc gate voltage. (d) The plot of sound velocity $V_s=\frac{f_0 l^2}{1.78r}$ calculated using the measured frequency ($\omega/2\pi$) of the fundamental mode of the InAs NW resonators and geometrical values. The dashed line indicates the speed of sound obtained for $V_s=\sqrt{E/\rho}$ using bulk values for E and ρ (Ref. 32).

the NW at the difference frequency ($\Delta\omega$), also called the mixing current $I_{mix}(\Delta\omega)$, can be written as[12]

$$I_{mix}(\Delta\omega) = I_{oscn}(\Delta\omega) + I_{back}(\Delta\omega) = \frac{1}{2}\frac{dG}{dq}\left(\frac{dC_g}{dz}z(\omega)V_g^{\mathrm{dc}} + C_g V_g(\omega)\right)V_{SD}, \quad (1)$$

where G is the conductance of the NW, q is the charge induced by the gate, C_g is the gate capacitance, $z(\omega)$ is the amplitude of oscillation at the driving frequency ω, and z axis is perpendicular to the substrate. The term $I_{back}(\Delta\omega) = \frac{1}{2}\frac{dG}{dq}C_g V_g(\omega)V_{SD}$ is the background mixing current which is independent of the oscillation of the NW and $I_{oscn}(\Delta\omega) = \frac{1}{2}\frac{dG}{dq}\frac{dC_g}{dz}z(\omega)V_g^{\mathrm{dc}}V_{SD}$ depends on the amplitude of oscillation. Measuring $I_{mix}(\Delta\omega)$ using a lock-in allows us to monitor the resonance of the NW as the frequency is swept. Figure 1(b) shows $I_{mix}(\Delta\omega)$ as a function of $\omega/2\pi$ for $V_g^{\mathrm{dc}}=\pm 36.4$ V (red circles for positive V_g^{dc} and blue triangles for negative V_g^{dc}). The sharp feature corresponds to the mechanical resonance of the NW. We address the asymmetry of the mixing current signal for $\pm V_g^{\mathrm{dc}}$ later. Figure 1(c) shows the plot of conductance (G) as a function of V_g^{dc}. The variation of G with V_g^{dc} is very critical for this scheme of heterodyne mixing to work as it controls the overall amplitude $I_{mix}(\Delta\omega)$. The hysteresis observed in the measurement of conductance is typical for our suspended devices and is associated with charge trap states with dipolar nature on surface of the nanowire.[30,31]

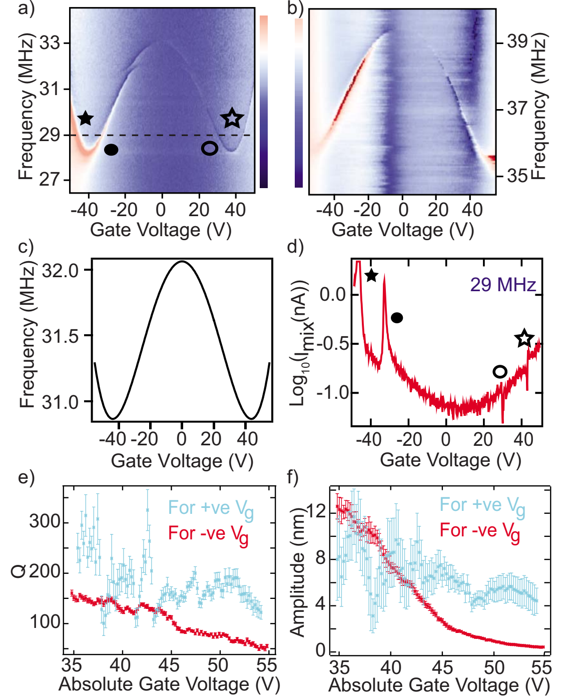

FIG. 2. (Color online) [(a) and (b)] Color logscale plots of mixing current as a function of V_g^{dc} and $\omega/2\pi$ for two devices [for device-1, Fig. 2(a), diameter d=100 nm, length l=2.9 μm and for device-2, Fig. 2(b), d=120 nm, l=3.1 μm]. (c) *Calculated* dispersion as a function of V_g^{dc}. (d) Line plot at 29 MHz for device-1 [dashed line in Fig. 2(a)]. (e) The plot of the Q as a function of V_g^{dc} for device-1. (f) The plot of the "amplitude" z_{amp}^{reso} as a function of V_g^{dc} for device-1. [The dark red (black) and light blue (light gray) traces in Figs. 2(e) and 2(f), show the data for negative and positive gate voltages.]

We can connect the resonant frequency of the fundamental mode, f_0, of a doubly clamped beam at zero V_g^{dc}, to the material properties of the beam as $f_0=C_0\frac{r}{l^2}V_s$ where $V_s=\sqrt{\frac{E}{\rho}}$ is the velocity of sound; r is the radius of the beam, l is the length of the beam, E is the Young's modulus, ρ is the density of the material, and C_0=1.78. Figure 1(d) shows a plot for V_s that does not vary much from the bulk value[32] (dashed line) for eight different devices. The scatter around the V_s calculated using bulk values could be due to the relative volume fraction contribution of the amorphous layer around the NWs; this needs further detailed study.

III. NONMONOTONIC FREQUENCY DISPERSION

Figures 2(a) and 2(b) show the color-scale plot of $I_{mix}(\Delta\omega)$ as a function of V_g^{dc} and $\omega/2\pi$ on a logscale spanning more than three decades. Data is taken by sweeping V_g^{dc} for each value of frequency. In the data from both the devices we see a symmetric evolution of the resonant frequency as a function of V_g^{dc}. The parabolic behavior is expected as the attractive force exerted by the gate on the wire is given by $F_{\mathrm{dc}}=\frac{1}{2}(V_g^{\mathrm{dc}})^2\nabla C_g$. An increase in V_g^{dc} enhances the tension in

the NW.[33] We now discuss the particular W-shaped dispersion of modes as a function of $V_g^{\rm dc}$. As $|V_g^{\rm dc}|$ is increased, initially the mode disperses negatively and after a certain threshold voltage V_g^{th} it disperses with a positive slope. Although purely negatively and positively dispersing modes have been studied in detail before by Kozinsky *et al.*,[34] we observe the crossover regime where these interactions compete. This particular dispersion can be understood using a toy model in which a wire is suspended from a spring of force constant K_i above the substrate. The wire and the substrate make up the two electrodes of a capacitor. There are two consequences of increasing $|V_g^{\rm dc}|$: first, it changes the equilibrium position by moving the NW closer to the substrate and second, it makes the local potential asymmetric and less steep. The effective force constant, K_{eff}, is reduced, resulting in negative dispersion of the mode for $|V_g^{\rm dc}|<|V_g^{th}|$. If the intrinsic force constant K_i had been independent of $V_g^{\rm dc}$, the modes would always disperse negatively when motion occurs perpendicular to the gate plane. However, in general K_i can be written as $k+\alpha(V_g^{\rm dc})^2+\beta(V_g^{\rm dc})^4+H.O.(V_g^{\rm dc})$; where k, α, and β are constants. With $V_g^{\rm dc}\neq 0$ then, to a first approximation, $K_{eff}=K_i-\frac{1}{2}(V_g^{\rm dc})^2\frac{d^2C_g}{dz^2}$. We find that the W shape of the dispersion curve can be explained only if one considers the case where $\beta>0$. The result of such calculations [Fig. 2(c)] quantitatively explains the experimental observations. V_g^{th}, the value at which the crossover from negative to positive dispersion occurs is a function of the dimensions of the NW and the capacitive geometry of the device. The effect of the device dimension is clearly seen in a larger value of V_g^{th} in device-2 shown in Fig. 2(b) where the doubly clamped beam is 120-nm thick, as against 100 nm for device-1 in Fig. 2(a) (the lengths differ by 200 nm).

Next, we consider another complementary aspect of the data—the amplitude of the mixing current. Figure 2(d) shows $I_{mix}(\Delta\omega)$ (logscale) as a function of $V_g^{\rm dc}$. We see that the amplitude of the mixing current for the negative values of $V_g^{\rm dc}$ are significantly larger than those for positive $V_g^{\rm dc}$ for the same mechanical mode; this is also seen in Fig. 1(b). We now try to understand this asymmetry as our InAs NW are *n*-type semiconductors[26] as seen in Fig. 1(c). To understand this asymmetry we have carried out detailed fits of the experimental data for the amplitude of mixing current as a function of frequency using Eq. (1). The amplitude $z(\omega)$ of oscillation at frequency ω is given by

$$z(\omega)=\frac{z_{amp}^{reso}}{Q}\frac{\cos\left[\Delta\phi+\arctan\left(\frac{\omega_0^2-\omega^2}{\omega\omega_0/Q}\right)\right]}{\sqrt{\left[1-\left(\frac{\omega}{\omega_0}\right)^2\right]^2+\left(\frac{\omega/\omega_0}{Q}\right)^2}}, \qquad (2)$$

where z_{amp}^{reso} is the amplitude at resonant frequency ω_0, Q is the quality factor, and $\Delta\phi$ is the relative phase difference between the ω and $\omega+\Delta\omega$ signals that depends on the device parameters such as the contact resistance. Fitting from Eqs. (1) and (2) allow us to extract the variation of Q as a function of $V_g^{\rm dc}$ as shown in Fig. 2(e) (see Appendix A). We have also estimated the amplitude of oscillation using Eqs. (1) and (2) by examining the ratio

$$\frac{I_{oscn}(\Delta\omega)}{I_{back}(\Delta\omega)}=\frac{\frac{dC_g}{dz}z(\omega)V_g^{\rm dc}}{C_gV_g(\omega)}.$$

A plot of the calculated amplitude (z_{amp}^{reso}) is seen in Fig. 2(f). We see that as the $|V_g^{\rm dc}|$ is increased Q and z_{amp}^{reso} are observed to decrease.

IV. CHARGE SCREENING AND FEM CALCULATION

We observe that there are noticeable differences in Q and z_{amp}^{reso} for positive and negative values of $V_g^{\rm dc}$ [light blue (light gray) color for positive and dark red (black) color for negative $V_g^{\rm dc}$ in Figs. 2(e) and 2(f)]. The values of Q and z_{amp}^{reso} are larger for positive $V_g^{\rm dc}$. One of the possible mechanisms that can explain this behavior in the amplitude is that with increasing $V_g^{\rm dc}$ one increases the density of electrons in the NW leading to reduction in the screening length. This implies that the simple geometrical capacitance is inaccurate particularly since the screening length can be comparable to NW diameter at low densities (at negative $V_g^{\rm dc}$ in our case). In our device geometry, using Thomas-Fermi approximation,[22] screening length is around 20–40 nm (diameter of our devices are 100 nm) and the distance between the nanowires and gate oxide is 200 nm. So, the screening length is a significant fraction of the diameter and the suspension distance—this plays a critical role in observing the effect of density gradients within the cross section of the nanowire. In case of single-walled carbon nanotube, diameter is 1–2 nm and height of suspension is typically 100 nm or more.[13–16] Additionally the screening length in carbon nanotubes is typically several multiples of the nanotube diameter[35] so due to an increased ratio of suspension distance to diameter and the large screening length compared to the diameter it is very difficult to observe the physics we discuss for the case of nanowires in carbon nanotubes. We would like to point out that this is not a peculiarity of the InAs nanowires and should be seen in other semiconducting nanowire devices as well with similar dimensions. Additionally, if one considers the realistic case with nonuniform density of carriers in the NW due to the device geometry[36] the NW will have a gradient of dielectric constant.[37] A gradient of dielectric constant[38] along with a change in capacitance as a function of the density changes the capacitive coupling of the NW to the gate. This results in differing amplitudes for two different electron densities. Our device geometry with NW diameter comparable to the gap accentuates this effect.

In order to better understand the effect of the gate voltage in tuning the spatial charge density across the cross section of the nanowire we self-consistently solve three-dimensional Poisson's equation using finite-element method for our device geometry. We use the approach followed by Khanal *et al.*[36] by solving $\nabla\cdot\epsilon_d\nabla\Phi(x,y,z)=\rho(x,y,z)$, throughout the space of the nanowire and its dielectric environment (here ϵ_d is dielectric constant, Φ is the local electrostatic potential in the system due to applied gate voltage, and ρ is space charge density inside the NW). The geometry consists of a 100-nm diameter and 1.5-μm long InAs nanowire clamped by metallic electrodes. The wire is suspended 100 nm above a 300-

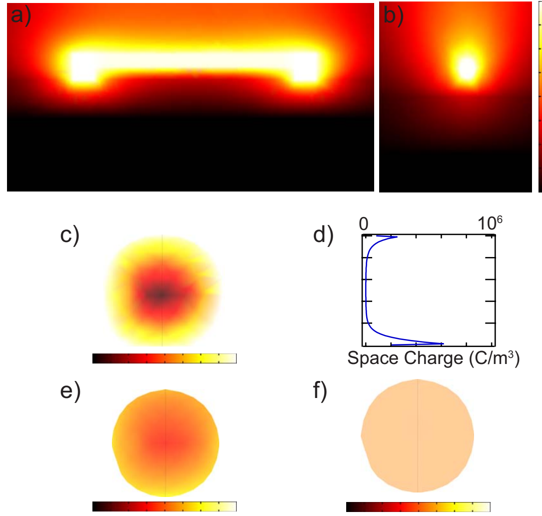

FIG. 3. (Color online) [(a) and (b)] Shows the result of a FEM based self-consistent solution of Poisson's equation giving the potential around a doubly clamped suspended nanowire device 100 nm in diameter and 1.5-μm long. The separation of the NW and 300-nm-thick SiO_2 is 100 nm. The back plane of the nanowire is the gate, held at −5 V and the two terminals of the wire are grounded. The maximum of the color-scale bar (white) is 0 V and the minimum (black) is −5 V. (c) The space charge distribution in the cross section of the nanowire for $V_g^{dc}=-25$ V shows the gradient. The log-color scale below varies from 10 C/m^3 (black) to 10^6 C/m^3 (white). (d) Plot of space charge density in the vertical direction at $V_g^{dc}=-25$ V through the middle of the wire. The asymmetry along the vertical direction due the gate below the wire is clearly seen. (e) The space charge distribution in the cross section of the nanowire for $V_g^{dc}=-5$ V shows the gradient. The log-color scale below varies from 10^3 C/m^3 (black) to 10^5 C/m^3 (white). (f) The space charge distribution in the cross section of the nanowire for $V_g^{dc}=5$ V is uniform as the electron density in the nanowire is increased when the nanowire field effect transistor is turned on. The log-color scale below varies from 10^3 C/m^3 (black) to 10^5 C/m^3 (white).

nm-thick silicon-oxide dielectric on the gate electrode. Inside the nanowire the $\rho(x,y,z)=e[N_d-n(\Phi)+p(\Phi)]$ where e is the charge in an electron, N_d is the density of the n-type dopants ($\sim 10^{16}$ cm^{-3}), $n(\Phi)$, and $p(\Phi)$ are the densities of electrons and holes. The unintentional source of n-type dopants in our growth is Si and C, from the metal organic precursors and are assumed to be uniformly distributed throughout the nanowire. A self-consistent calculation gives us the distribution of potential throughout the space and space charge density in the nanowire. Figures 3(a) and 3(b) show the color-scale distribution of potential when the $V_g^{dc}=-5$ V. In order to model the consequences of modifying gate voltage we calculated the distribution of space charge density through the nanowire for $V_g^{dc}=-25$, −5, and 5 V. Figures 3(c)–3(f) show the result of such a calculation for varying V_g^{dc} for space charge density in the center of the NW. For positive voltages the Fermi energy is very close to the conduction band of the InAs and as a result the charge density is very uniform while behaving as a metal-like system. This simple modeling supports our arguments that a gradient of electron density can modify the capacitive coupling and the resulting amplitude. Further analysis is needed to solve self-consistent solutions to the Poisson's equation where the dielectric constant is itself a function of the density and the quantitative variation in Q and amplitude with sign of V_g^{dc}. Our measurements suggest a way to tune the efficiency of actuation by tuning the density of carriers.

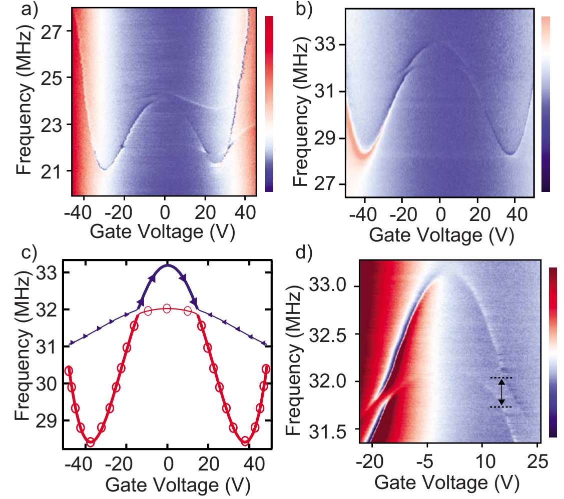

FIG. 4. (Color online) [(a) and (b)] Shows mode mixing for device-3 and device-1, respectively (for device-3, $d=103$ nm, and $l=3.1$ μm). (c) Calculated dispersion for mode mixing using asymmetry in the wire (see Appendix B). (d) Zoomed-in view for device-1 [Fig. 4(b)] which shows the mixing of the modes as a function of V_g^{dc}. Minimum separation between the modes, indicated by the double-headed arrow, is 0.25 ± 0.02 MHz.

V. MODE MIXING AND NONLINEAR OSCILLATIONS

We next consider three other features of our data—first, the presence of other mechanical modes near the fundamental mode; second, the mixing of modes as a function of the V_g^{dc}, and third, the nonlinear properties of NW oscillators driven to large amplitudes. Figures 4(a) and 4(b) show the plot of $I_{mix}(\Delta\omega)$ as a function of V_g^{dc} and $\omega/2\pi$ for device-3 and device-1. It is well known that for a doubly clamped beam with no tension, $f_n=C_n\frac{r}{l^2}\sqrt{\frac{E}{\rho}}$ with $C_0=1.78$, $C_1=4.90$, and $C_2=9.63$ for the transverse modes. It is clear that if the fundamental mode (f_0) is described by a mode with zero nodes and moving in a plane perpendicular to the substrate, the other observed modes, in the frequency range near f_0 [Figs. 4(a) and 4(b)], cannot be defined by f_1 and f_2. We have observed the anticipated f_1 and f_2 modes at higher frequencies. The other modes beside the fundamental in Figs. 4(a) and 4(b), are explained due to geometrical asymmetry along the diameter in the NW [Fig. 4(c), details of this calculation provided in Appendix B]. These are the modes involving motion in a plane that is not perpendicular to the substrate. This would explain the less steep slope of the dispersion as a function of V_g^{dc}.

Figures 4(a) and 4(b) also show the mixing of the modes as a function of V_g^{dc}. The mode mixing can be seen clearly in Fig. 4(d) which shows a closeup of the data in Fig. 4(b). Displacement along the transverse direction y (perpendicular to z) will weakly affect the capacitance because of any slight

asymmetry in the physical structure of the NW. The coupling coefficient $\frac{1}{2}\frac{\partial^2 C}{\partial z \partial y}(V_g^{dc})^2$ appearing in the potential energy gives rise to mode mixing (see Appendix B). For the device shown in Fig. 4(b) the minimum frequency gap in the region of level repulsion is 0.25 ± 0.02 MHz. The asymmetry in the amplitude of the modes away from the region of mixing can also be understood within this model.

We next consider the nonlinear response of these NEMS oscillators. Due to electrostatic actuation, the potential energy of the oscillator is asymmetric about the equilibrium position and has the form $V(z)=\frac{1}{2}K_{eff}z^2+\theta z^3+\mu z^4+H.O.(z)$, where K_{eff}, θ, and μ are coefficients depending on V_g^{dc}. We have experimentally probed the nonlinear and hysteretic response of the device. Figures 5(a)–5(d), show the experimentally measured nonlinear response of device-1 leading to hysteretic behavior as function of V_g^{dc} with increasing amplitude of driving force. Here, V_g^{dc} is swept at a given drive frequency to measure the mixing current and several such V_g^{dc} sweeps are collated (the distinct response of sweeping the frequency at a fixed V_g^{dc}—a common mode to study nonlinear response—is described in Appendix C). There are two features that we would like to point out—first, in the region at the bottom of the W-shaped dispersion curve, two branches of the same mode merge into one broad peak where the oscillator has large amplitude over a wide range of V_g^{dc} and second, whenever during the V_g^{dc} sweep, one crosses the region with a local negative value for $\frac{df_0}{dV_g^{dc}}$ (here, f_0 is the resonant frequency at a particular V_g^{dc}), shows a curved hysteretic j-shaped response (indicated by ⋆), seen in Fig. 5(b). In order to understand and explain the experimentally observed hysteretic response as a function of V_g^{dc}, we have used the Duffing equation[39] for our resonator. The result of such a calculation for amplitude is seen in Figs. 5(e)–5(h) with increasing amplitude of driving force. To calculate the amplitude we have only used the observed dispersion relation (W shape) as input for Duffing equation. There is a qualitative agreement between the experimentally measured data shown in Figs. 5(a)–5(d) and results of calculation using the Duffing equation shown in Figs. 5(e)–5(h). We find that for every increase in excitation amplitude by 100 mV corresponds to an increase on a factor of 2.5 in the anharmonic component of the Duffing equation (from observing the calculated data). Additional aspect of the nonlinearity of the oscillator is also seen in the evolution of dispersion near $V_g^{dc}=0$ as the actuation amplitude is gradually increased from 100 to 400 mV in Figs. 5(a)–5(d). The negative dispersion is due to the softening of electrostatic force and with larger amplitude of oscillation the effective spring constant changes, as the wire samples a region with varying electric field; this difference is clearly seen in the dispersion near $V_g^{dc}=0$ for the data shown in Figs. 5(a) and 5(d).

Figure 5(i), shows the line plot [along the dashed line in Fig. 5(f)] of calculated amplitude for different sweep direction of V_g^{dc} and the resulting hysteresis. The observed hysteretic response, as a function of V_g^{dc}, is quite different from the hysteretic response as a function of drive frequency (discussed in Appendix C). This nonlinear response of our devices with V_g^{dc} may be utilized for charge detection[24] as near the onset of nonlinearity the change in amplitude as a function of V_g^{dc} is very large.

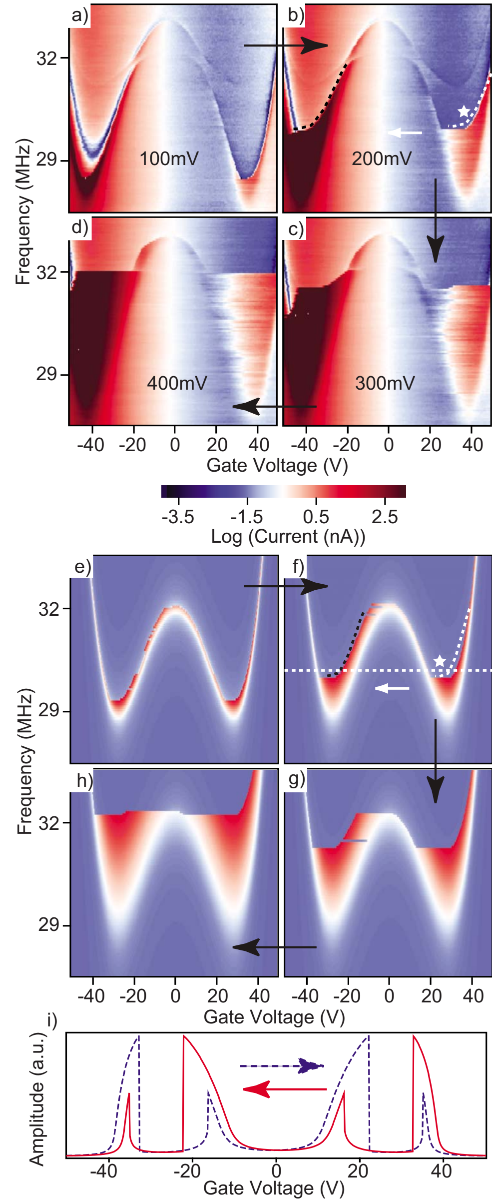

FIG. 5. (Color online) [(a)–(d)] Color logscale plots of mixing current from device-1 as a function of V_g^{dc} and $\omega/2\pi$ in nonlinear regime with increasing amplitude of driving force starting from 100 to 400 mV, respectively. [(e)–(h)] Color-scale plots of calculated amplitude of a resonator in the nonlinear regime using Duffing equation with increasing amplitude of driving force from Figs. 5(e)–5(h). (i) Shows the amplitude for the two directions of V_g^{dc} (solid red and dashed blue lines) which indicates hysteresis at constant frequency 31 MHz (solid red and dashed blue arrows show corresponding gate sweep direction).

VI. CONCLUSIONS

In summary, we have studied the electromechanical properties of doubly clamped InAs NW resonators. Their size and tunable electron density allow us to map behavior that has not been manifested earlier in a single device. We have observed and quantitatively explained the competition between the softening of stiffness of the restoring force of the resonator and increase in tension due to the variation in the elec-

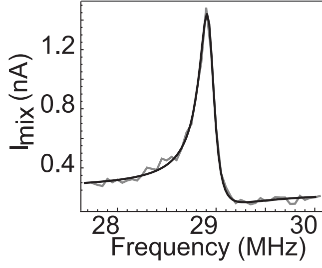

FIG. 6. Shows fitting of measured data.

trostatic force under variable gate voltage. At larger voltages, the stretching of the nanowire leads to increased stiffness resulting in a nonmonotonic dispersion of the fundamental mode with V_g^{dc}. The screening of electric fields due to the change in the density of the electrons in our suspended FET devices modifies the amplitude because the variation in the screening length spans the cross-sectional dimension of our nanowire. Further, the nonlinear properties of our device can be understood qualitatively using the Duffing equation that explains the hysteretic response of the amplitude as a function of gate voltage. Thus in a single device, we demonstrate, separate and account for three diverse behaviors. Our measurements indicate that measuring electromechanical response influenced by charge screening could lead, in the future, to new ways to probe spin physics by exploiting spin-dependent charge screening.[40] Probing the physics by tuning electron density in NEMS devices may help probe the role of defects[41] and electron hopping as one moves from insulating to conducting regimes. Control over the nonlinear dynamics may be achievable by controlling mode mixing and dc gate voltage.

ACKNOWLEDGMENT

This work was supported by Government of India. J. Parpia was supported under NSF Grant No. DMR-0457533.

APPENDIX A: QUALITY FACTOR, Q AND AMPLITUDE OF VIBRATION, z_{amp}^{reso}

To extract quality factor Q and amplitude of vibration z_{amp}^{reso}, we fit Lorentzian line shape of measured data using Eqs. (1) and (2) of main text (Fig. 6). The Q of our devices are low. We think there the reason for low Q is that in our devices gold, a soft metal, is the clamping material, which may lead to some clamping losses. Some preliminary measurements have been made by coating the NWs with Al_2O_3 and the Q is observed to improve.

APPENDIX B: COUPLING OF MODES

If we assume that there are asymmetries in the cross section of the nanowire then the capacitance C will depend not only on the coordinate in the direction perpendicular to the gate plane (z axis) but also on the transverse direction (y axis) parallel to the gate plane and perpendicular to the NW.

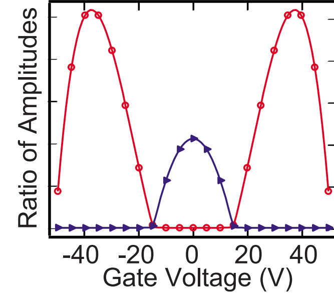

FIG. 7. (Color online) Shows the calculated ratio of z and y—amplitudes of two modes (red circles and blue triangles) for natural oscillations as V_g^{dc} is swept.

The motion in the transverse y direction will be weakly affected by the gate voltage V_g^{dc} as compared to motion perpendicular to the gate plane.

For small oscillations[42] (at frequency f) about equilibrium with two degrees of freedom (z and y), the matrix of coefficients appearing in the Hamiltonian takes the form

$$\begin{pmatrix} 4\pi^2 m f^2 - K_i^z + \frac{1}{2}\frac{\partial^2 C}{\partial z^2}(V_g^{dc})^2 & \frac{1}{2}\frac{\partial^2 C}{\partial z\,\partial y}(V_g^{dc})^2 \\ \frac{1}{2}\frac{\partial^2 C}{\partial y\,\partial z}(V_g^{dc})^2 & 4\pi^2 m f^2 - K_i^y + \frac{1}{2}\frac{\partial^2 C}{\partial y^2}(V_g^{dc})^2 \end{pmatrix}$$

K_i^z and K_i^y are the intrinsic force constants for motion along z and y directions, respectively.

K_i^z and K_i^y are assumed to depend upon V_g^{dc} in a way similar to what we have discussed earlier.

$$K_i^z = k^z + \alpha^z (V_g^{dc})^2 + \beta^z (V_g^{dc})^4,$$

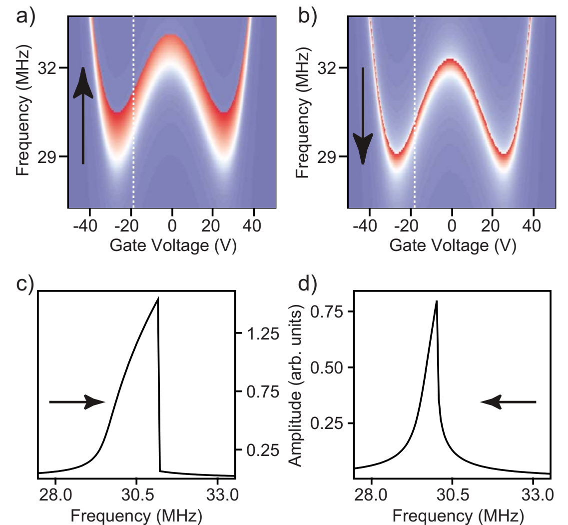

FIG. 8. (Color online) [(a) and (b)] Color-scale plots of calculated amplitude of a resonator in the nonlinear regime using Duffing equation for increasing and decreasing frequency sweeps, respectively. [(c) and (d)] Show the line plots of dashed line in 8a and 8b, respectively. Arrows are showing frequency sweep direction.

$$K_i^y = k^y + \alpha^y (V_g^{dc})^2 + \beta^y (V_g^{dc})^4.$$

The nonzero off-diagonal element $\frac{1}{2}\frac{\partial^2 C}{\partial z \partial y}(V_g^{dc})^2$ in the matrix of coefficients mentioned above gives rise to coupling of the two modes and their mixing.

In our experimental data, for a certain value of gate voltage V_g^{dc}, one mode appears prominently while the other is comparatively faint. Only close to the region of level repulsion they are equally prominent. The mode for which the amplitude of oscillation is larger in z direction than in y shows up more clearly in our detection scheme. This is explained by our model (Fig. 7). The ratio of amplitudes in z and y directions is higher for the blue mode (triangles) at lower gate voltages before mixing, and for the red mode (circles) after mixing. However, we do not see mode mixing in all the devices (e.g., device-2) because this coupling due to asymmetry is dependent on the structure of the NW and may be negligible in many cases.

APPENDIX C: HYSTERESIS IN FREQUENCY SWEEP

In the main text, we discussed the hysteresis in nonlinear regime with V_g^{dc} (Fig. 5). We have simulated the response of the oscillator in the nonlinear regime by writing a program based on the Duffing equation incorporating the effect of nonmonotonic frequency dispersion. Figure 8 shows the calculated amplitude of resonance as frequency is swept up and down.

*deshmukh@tifr.res.in

[1] K. L. Ekinci and M. L. Roukes, Rev. Sci. Instrum. **76**, 061101 (2005).
[2] R. G. Knobel and A. N. Cleland, Nature (London) **424**, 291 (2003).
[3] Y. T. Yang, C. Callegari, X. L. Feng, K. L. Ekinci, and M. L. Roukes, Nano Lett. **6**, 583 (2006).
[4] K. Jensen, K. Kim, and A. Zettl, Nat. Nanotechnol. **3**, 533 (2008).
[5] B. Lassagne, D. Garcia-Sanchez, A. Aguasca, and A. Bachtold, Nano Lett. **8**, 3735 (2008).
[6] H.-Y. Chiu, P. Hung, H. W. C. Postma, and M. Bockrath, Nano Lett. **8**, 4342 (2008).
[7] G. Zolfagharkhani, A. Gaidarzhy, P. Degiovanni, S. Kettemann, P. Fulde, and P. Mohanty, Nat. Nanotechnol. **3**, 720 (2008).
[8] D. Rugar, R. Budakian, H. J. Mamin, and B. W. Chui, Nature (London) **430**, 329 (2004).
[9] J. N. Munday, F. Capasso, and V. A. Parsegian, Nature (London) **457**, 170 (2009).
[10] M. D. LaHaye, O. Buu, B. Camarota, and K. C. Schwab, Science **304**, 74 (2004).
[11] C. A. Regal, J. D. Teufel, and K. W. Lehnert, Nat. Phys. **4**, 555 (2008).
[12] V. Sazonova, Y. Yaish, H. Ustunel, D. Roundy, T. A. Arias, and P. L. McEuen, Nature (London) **431**, 284 (2004).
[13] G. A. Steele, A. K. Huttel, B. Witkamp, M. Poot, H. B. Meerwaldt, L. P. Kouwenhoven, and H. S. J. van der Zant, Science **325**, 1103 (2009).
[14] B. Lassagne, Y. Tarakanov, J. Kinaret, D. Garcia-Sanchez, and A. Bachtold, Science **325**, 1107 (2009).
[15] A. K. Huttel, G. A. Steele, B. Witkamp, M. Poot, L. P. Kouwenhoven, and H. S. J. van der Zant, Nano Lett. **9**, 2547 (2009).
[16] A. K. Huttel, B. Witkamp, M. Leijnse, M. R. Wegewijs, and H. S. J. van der Zant, Phys. Rev. Lett. **102**, 225501 (2009).
[17] J. S. Bunch, A. M. van der Zande, S. S. Verbridge, I. W. Frank, D. M. Tanenbaum, J. M. Parpia, H. G. Craighead, and P. L. McEuen, Science **315**, 490 (2007).
[18] C. Chen, S. Rosenblatt, K. I. Bolotin, W. Kalb, P. Kim, I. Kymissis, H. L. Stormer, T. F. Heinz, and J. Hone, Nat. Nanotechnol. **4**, 861 (2009).
[19] D. Garcia-Sanchez, A. M. van der Zande, A. S. Paulo, B. Lassagne, P. L. McEuen, and A. Bachtold, Nano Lett. **8**, 1399 (2008).
[20] X. L. Feng, R. He, P. Yang, and M. L. Roukes, Nano Lett. **7**, 1953 (2007).
[21] D. W. Carr, S. Evoy, L. Sekaric, H. G. Craighead, and J. M. Parpia, Appl. Phys. Lett. **75**, 920 (1999).
[22] C. T. Black and J. J. Welser, IEEE Trans. Electron Devices **46**, 776 (1999).
[23] M. Stengel and N. A. Spaldin, Nature (London) **443**, 679 (2006).
[24] H. Krommer, A. Tilke, S. Manus, and R. H. Blick, Europhys. Lett. **50**, 101 (2000).
[25] X. Duan and C. M. Lieber, Adv. Mater. (Weinheim, Ger.) **12**, 298 (2000).
[26] S. Dhara, H. S. Solanki, V. Singh, A. Narayanan, P. Chaudhari, M. Gokhale, A. Bhattacharya, and M. M. Deshmukh, Phys. Rev. B **79**, 121311(R) (2009).
[27] V. Sazonova, Ph.D. thesis, Cornell University, 2006.
[28] R. Knobel, C. S. Yung, and A. N. Cleland, Appl. Phys. Lett. **81**, 532 (2002).
[29] R. He, X. L. Feng, M. L. Roukes, and P. Yang, Nano Lett. **8**, 1756 (2008).
[30] S. A. Dayeh, C. Soci, P. K. L. Yu, E. T. Yu, and D. Wang, Appl. Phys. Lett. **90**, 162112 (2007).
[31] H. Y. Li, O. Wunnicke, M. T. Borgstrom, W. G. G. Immink, M. H. M. van Weert, M. A. Verheijen, and E. P. A. M. Bakkers, Nano Lett. **7**, 1144 (2007).
[32] M. Levinshtein, *Handbook Series On Semiconductor Parameters* (World Scientific, Singapore, 1996), Vol. 1.
[33] S. Sapmaz, Y. M. Blanter, L. Gurevich, and H. S. J. van der Zant, Phys. Rev. B **67**, 235414 (2003).
[34] I. Kozinsky, H. W. C. Postma, I. Bargatin, and M. L. Roukes, Appl. Phys. Lett. **88**, 253101 (2006).
[35] K. Sasaki, Phys. Rev. B **65**, 195412 (2002).
[36] D. R. Khanal and J. Wu, Nano Lett. **7**, 2778 (2007).
[37] P. K. W. Vinsome and D. Richardson, J. Phys. C **4**, 2650 (1971).
[38] Q. P. Unterreithmeier, E. M. Weig, and J. P. Kotthaus, Nature (London) **458**, 1001 (2009).
[39] L. Landau and E. Lifshitz, *Course of Theoretical Physics: Mechanics* (Butterworth-Heinemann, Oxford, 1976), Vol. 1.
[40] S. Zhang, Phys. Rev. Lett. **83**, 640 (1999).
[41] N. A. Poklonski and V. F. Stelmakh, Phys. Status Solidi B **117**, 93 (1983).
[42] H. Goldstein, C. Poole, and J. Safko, *Classical Mechanics* (Pearson Education, Singapore, 2004).